Engineering Fracture Mechanics 78 (2011) 2097–2114

Contents lists available at ScienceDirect

Engineering Fracture Mechanics

journal homepage: www.elsevier.com/locate/engfracmech

J–Q characterized stress fields of surface-cracked metallic liners – II. Composite overwrapped pressure vessels

Shawn A. English [a], Nagaraj K. Arakere [a,*], Phillip A. Allen [b]

[a] *Department of Mechanical & Aerospace Engineering, University of Florida, Gainesville, FL, USA*
[b] *NASA Marshall Space Flight Center, MSFC, Huntsville, AL, USA*

ARTICLE INFO

Article history:
Received 27 October 2010
Received in revised form 21 February 2011
Accepted 23 February 2011
Available online 22 April 2011

Keywords:
Constraint effects
Finite element analysis
Ductile fracture
J-integral
Pressurized components

ABSTRACT

Two-parameter *J–Q* elastic–plastic crack front fields are developed for surface-cracked metallic liners of composite overwrapped pressure vessels (COPV). Uniaxial tensile data from 6061-T6 aluminum coupon specimens for the metallic liner and anisotropic elastic material properties for the filament wound carbon fiber epoxy are used in three-dimensional finite element models. Modified boundary layer (MBL) finite element solutions are used to evaluate near tip dominance and parameterization limits. Semicircular surface cracks of varying depths inserted in the inner liner surface are investigated. *J* and *Q* crack front distributions, and the corresponding parameterization limits, and near tip triaxiality trends are obtained and the effects of elastic–plastic material discontinuity of the heterogeneous joint and the biaxiality of stresses are evaluated. *J–Q* predicted fields maintain accuracy for higher far-field loads and lower near tip deformations compared to the liner only models for angles near the free surface. However, for the critical crack growth region, *Q* does not maintain a radially independent measure of constraint for loads seen in a typical COPV; therefore, these fracture predictors may not be applicable. In the COPV, large-scale yielding marks a transition where triaxiality is higher as a function of constraint compared to the linear relationship common to homogeneous structures. Results from this study will facilitate the implementation of proof test logic and accurate fracture prediction of COPV liners with emphasis on geometric limits and fracture specimen applicability.

1. Introduction

Methodology for load based two-parameter limits of surface cracks in a metallic liner of a uniaxial tension metallic/composite bonded geometry is presented in a part I paper in *Engineering Fracture Mechanics* titled "*J–T* characterized stress fields of surface-cracked metallic liners bonded to a structural backing-I. Uniaxial tension" [1]. The results presented in that study demonstrate the strong dependency of near tip fields referenced to *J–T* Modified Boundary Layer (MBL) predictions on the elastic–plastic discontinuities of a bonded structure.

As in the abovementioned preliminary study, the fracture prediction of a bonded structure is of intrinsic and practical interest with application in composite overwrapped pressure vessels (COPV). COPVs have found wide use in many space propulsion systems at NASA. They are made up of a thin metallic inner liner wrapped with a comparatively thick (greater than three times the liner thickness) filament wound composite. The overwrap serves as the primary structural component, with the liner supporting very little load. A through flaw in the metallic liner of a COPV is assumed detectable by leakage in proof testing due to the porous structure of the filament wound composite overwrap. Therefore, surface cracks are the most critical

* Corresponding author. Tel.: +1 352 392 0856; fax: +1 352 392 1071.
E-mail addresses: shawn350@ufl.edu (S.A. English), nagaraj@ufl.edu (N.K. Arakere), phillip.a.allen@nasa.gov (P.A. Allen).

0013-7944/$ - see front matter © 2011 Elsevier Ltd. All rights reserved.
doi:10.1016/j.engfracmech.2011.02.023

Nomenclature

t_L	thickness of the metallic liner
t_{Hel}	thickness of the helical overwrap layer
t_{Hoop}	thickness of the hoop overwrap layer
a	crack depth
c	half crack width
r	radial distance from crack tip
d_i	inner pressure vessel diameter
d_o	outer pressure vessel diameter
θ	angle in plane perpendicular to crack front, θ=0° is in the growth direction of the crack plane
ϕ	angle measured along the crack front in the crack plane
β	wrap angle measured from the longitudinal direction on the outer pressure vessel surface
σ_y	0.2% offset yield strength
σ_o	reference stress (σ_o=σ_y for this study)
σ_∞	nominal equivalent (von-Mises) stress of metallic section without crack (far-field)
J	J-integral
T	T-stress
Q	stress difference constraint parameter

flaws in terms of limiting structural life for liners during normal operation when proof cycles and crack detection techniques have been exhausted. Proof test logic for COPVs is not well established and is primarily focused on the failure of the overwrap characterized by burst or the leakage of a through crack in the liner, while the growth of a surface crack is not well understood. Understanding the behavior of surface cracks in COPV liners for the development of proof test logic is challenging because the partial elasticity of the structure imposes complex constraint conditions significantly affecting the near tip fields. Additionally, plastic deformation of the liners during manufacturing processes and normal operation facilitate the plastic collapse of near tip fields and a transition to the ductile tearing growth mechanism, especially in aluminum liners.

It is desirable to use established fracture parameterizations to predict fracture and crack growth characteristics of surface cracks in the liners. Fracture prediction for through-thickness cracks has been studied extensively using single parameter (K for brittle fracture and J for ductile fracture) characterizations. However, with the onset of large-scale yielding, the J-integral alone does not uniquely describe the crack tip fields when constraint effects arising from geometry and load configuration are considered. A second parameter is introduced to quantify the crack tip constraint. In-plane constraint, typically quantified by T-stress or Q, is influenced by the specimen dimension in the direction of crack growth and by global load configuration.

In our part I paper [1], the applicable limits of J–T two-parameter characterization of elastic–plastic crack-tip fields using MBL solutions were investigated for the bonded uniaxial surface crack geometry. This type of methodology has been explored by many investigators [2–4]. Wang [3] extended the two-parameter characterization with MBL reference solutions to topographical planes perpendicular to the crack front in surface crack tension (SC(T)) and surface crack bend (SC(B)) geometries. Elastically scaled T-stresses calculated from far-field loads in elastic–plastic models are a relatively accurate constraint measurement for two-parameter characterization [4]. T-stress however is not defined under fully yielded conditions and therefore cannot provide a clear definition of field collapse under large deformations where the near tip fields are characteristic of J dominance but exceed elastic limits of the constraint measure.

O'Dowd and Shih [5,6] introduce the constraint parameter Q to describe the configuration dependence of fracture response under large-scale yielding conditions. Wang [7] investigated Q as a function of load and radial distance from the crack tip for surface crack uniaxial and biaxial tension models. He showed that the Q parameter as a measure of the difference between the actual opening stress and the small-scale yielding solution is accurate for loads exceeding yield. The Q stress difference factor has been found to maintain a linear relationship with near tip triaxiality independent of geometry, dimensions and deformation level, where triaxiality is measured as the ratio of hydrostatic stress to von-Mises stress. Moreover, the Q factor is shown to accurately predict near tip stress and strain fields, particularly plastic strains, and therefore can be used as a ductile fracture parameter [8,9].

The construction of a two-parameter failure locus, commonly the critical J value as a function of Q, is necessary for engineering applications because it provides a more adjusted assessment of the failure limits [10,11]. Multiple experimental verifications of the constraint effects on critical crack driving force can be found in literature. Faleskog [12], Chao et al. [13] and MacLennan and Hancock [14] demonstrate the constraint effects on critical J values and resistance curves. In general, it has been shown that an increase in constraint results in a decrease in the critical value of J and crack growth resistance. For a fully adjusted surface crack failure criterion of COPV liners, it is necessary to construct a two-parameter failure locus that covers a large range of possible constraint levels especially when the biaxial stress fields produce a slightly positive constraint near the free surface to highly negative at crack depth.

This study will investigate the overwrap effects on constraint and crack driving force, near tip opening stress field characterizations limits, constraint loss and near tip triaxiality along with a comparison of *T*-predicted fields in homogeneous pressure vessels (liner only models) and COPVs. This will assess the applicability of the *J* and *Q* parameters for predicting fracture with complex constraint conditions and high loads seen in a sub-scale COPV specimen and a typical full-scale COPV. Although many geometries and material combinations exist, assessing these characteristics will aid in standardizing methodology for COPV failure prediction and development of proof test logic.

2. Background

2.1. Two-parameter fracture theory

The method of comparing one or two-parameter failure criteria to test specimens is reliant upon the ability to predict the elastic–plastic stress and strain fields near the crack tip. The parameterization limits for the analysis of standard test specimens and structures undergoing large deformations and constraint loss, such as the surface crack tensile specimen and a surface cracked COPV liner is necessary to accurately construct and apply a two-parameter failure locus for engineering applications. Within the limits of characterization, where two-parameter stress fields are assured, failure prediction can be made by comparing structural parameters to a conservative material dependent failure locus. Near tip stress fields will not maintain two-parameter dominance for loads exceeding deformation limits, thus the physical meaning of the fracture parameters is lost and may not produce a repeatable critical value.

2.2. J–Q theory

Two-parameter characterization uses a measure of the asymptotic fields, such as the stress intensity factor *K* or the *J*-integral with a constraint parameter, such as the *T*-stress or stress difference *Q*, to predict crack-front stress fields. Constraint *Q* is defined as the difference between the actual hoop stress ($\sigma_{\theta\theta}$) and a reference hoop stress within a cracked body. The small-scale yielding (SSY) hoop stress field, defined in modified boundary layer (MBL) solutions when the *T*-stress is zero, is used as the reference [15]. O'Dowd and Shih [5,6] showed that *Q* defines a hydrostatic shift of near tip stress fields. The corresponding equation is shown to be valid within a range of near tip normalized radial distances $1.5 \leqslant r/(J/\sigma_o) \leqslant 5$, where both cleavage and ductile fracture mechanisms are active and outside the area where finite strain effects are significant [7]:

$$\sigma_{ij}(r,\theta) = \left[\sigma_{ij}\left(\frac{r}{J/\sigma_o},\theta\right)\right]_{T=0} + Q\sigma_o\delta_{ij} \text{ for } -\pi/2 \leqslant \theta \leqslant \pi/2 \tag{1}$$

where the first term is the SSY solution, δ_{ij} is the Kronecker delta and σ_o is the reference or yield stress.

Silva et al. [11] showed that near tip analysis of plane strain cracked geometries produce relatively unchanged *Q* values when the normalized radial distance from the crack tip is varied between $1 \leqslant r/(J/\sigma_o) \leqslant 5$. Consequently, MBL solutions maintain constant *Q* values in this range. Surface crack front fields, where the points are embedded entirely in material ($\phi \leqslant 5$), are shown to conform to a state of plane strain as *r* approaches zero because the out of plane (parallel to the crack front) strains become small when compared to in-plane strains [16,17]. However, Bass et al. [18] shows that under biaxial loading, the opening stress difference fields do not correspond to the hydrostatic shift proposed by O'Dowd and Shih [5,6] indicated by the dependencies of *Q* on radial distance. Similarly, Wang [7] shows that for deep surface cracks ($a/t = 0.6$) under biaxial and uniaxial tension, *Q* fails to remain radially independent for angles close to the free surface at large deformations. English et al. [19] showed that material strain hardening greatly influences the radial dependency of *Q* under large-scale yielding in surface cracked geometries. They showed that low strain hardening materials, such as aluminum alloys or pressure vessel steels, fail to maintain a radially independent measure of *Q* for substantially lower levels of near tip deformations compared to a higher strain hardening material. The radial dependency of *Q* must be evaluated to assess its applicability as a ductile fracture parameter. Comparing opening stresses at two or more $r/(J/\sigma_o)$ values to those predicted using a *J*–*Q* MBL approach essentially measures the dependencies of *Q* on radial distance and can be used to evaluate *J*–*Q* dominance in structures [20].

The *Q*-parameter is commonly defined as the as the normalized hoop stress in the crack plane (σ_{yy}/σ_o) minus the SSY solution, where $T = 0$, at a normalized radial distance $r = 2J/\sigma_0$. This location is associated with the initiation of the cleavage mechanism and often is in the region of maximum opening stress [11].

$$Q = \frac{\sigma_{yy} - (\sigma_{yy})_{T=0}}{\sigma_o} \quad \text{at } \theta = 0 \text{ and } r/(J/\sigma_o) = 2 \tag{2}$$

A plane-strain *J*–*Q* family of fields is constructed using MBL finite element formulation. Therefore, *Q* is defined as a ductile fracture parameter and represents a material dependent near crack stress field as a function of $r/(J/\sigma_o)$.

2.3. Modified boundary layer solutions

Where linear elastic fracture mechanics facilitates analytical near tip stress field solutions, elastic–plastic near tip fields for an arbitrary material model must be formulated using MBL finite element models. The remote tractions for MBL formulation are given by the first two terms of the Williams eigen-expansion [21]:

$$\sigma_{ij}(r,\theta) = \frac{K_I}{\sqrt{2\pi r}} f_{ij}(\theta) + T\delta_{1i}\delta_{1j} \tag{3}$$

where K_I is the mode I stress intensity factor and T is the T-stress. These fields are applied as displacement boundary conditions to the outer boundary of the circular crack tip region. The corresponding in-plane displacements are given by:

$$u_i(r,\theta) = \frac{K_I}{E}\sqrt{\frac{r}{2\pi}} g_i(\theta,\nu) + \frac{T}{E} r h_i(\theta,\nu) \tag{4}$$

where E and ν are material constants and g_i and h_i are the angular variations in displacement caused by elastic singularity fields and T-stresses respectively [4]. Fig. 1 shows the half-symmetric FE mesh with plane-strain boundary conditions used for MBL analysis.

MBL solutions for elastic–plastic crack tip fields are obtained by applying these boundary conditions and varying the T-stress while K_I remains constant. Under contained plasticity, the J-integral simplifies correlatively to K, and the stress fields within the plastic zone are uniquely defined by the J-scaled length parameter ($r/(J/\sigma_o)$) and a measure of constraint (T or Q). The J-integral is related to the stress intensity factor K_I in plane strain by:

$$J = \frac{1-\nu^2}{E} K_I^2 \tag{5}$$

Abaqus version 6.7 is used to compute the MBL solutions [22]. Fig. 2 shows the near tip opening stress MBL reference fields for the 6061-T6 aluminum used in the liner FEA models. The 6061-T6 aluminum flow curve, necessary for MBL formulation, is given in the subsequent section.

An elastically scaled T-stress can be used to predict near tip stress fields up to and exceeding net-section yield in a surface cracked tensile geometry [3], however the physical meaning of T is lost with the onset of large-scale plastic deformation. For this study, the Q factor, which is calculable at loads exceeding yield, will be used in constraint loss and parameterization limit analysis. Fig. 3 shows the relationship between T and Q in MBL formulation. The near tip reference stress fields can be formulated for use in limit analysis as a function of T-stress or Q for constant normalized radial distances. Fig. 4a and b give these curves for $r/(J/\sigma_o) = 2$, 4, 6, and 8 as functions of T and Q respectively.

3. Finite element models

3.1. Materials description

The pressure vessel data and material properties were obtained through Carleton Technologies Inc. under the guidance of the NASA Engineering & Safety Center (NESC) Composite Pressure Vessels Working Group with the NASA Langley Research Center (LARC). All material properties are normalized for proprietary reasons.

A common material for COPV liners is 6061-T6 aluminum. Load displacement data from a uniaxial tensile plate ($t = 2.29$ mm) specimen of the liner material is used to construct the stress strain material flow curve. The material properties were calculated as follows: $E/\sigma_y = 267.5$ and $\nu = 0.33$, where E is Young's modulus, σ_y is the 0.2% offset yield strength and ν is Poisson's ratio. For the purposes of normalization and plasticity length scale estimations, the reference stress will be defined as the 0.2% offset yield strength ($\sigma_o = \sigma_y$). The resultant curve is discretized into stress and plastic strain inputs for the FEA model with a high concentration of points in the region of initial plastic strains. The stress strain specimen data and the

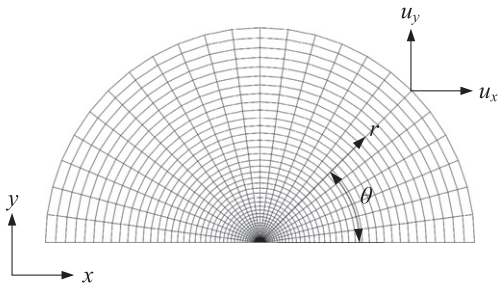

Fig. 1. Modified boundary layer (MBL) model mesh and displacement boundary conditions.

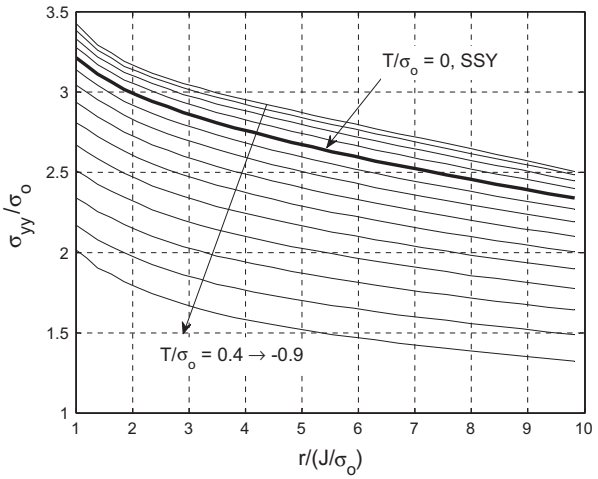

Fig. 2. MBL generated near tip opening stresses as a function of normalized radial distance $r/(J/\sigma_o)$ for a series of T-stresses ranging from $T/\sigma_o = 0.4$ to -0.9.

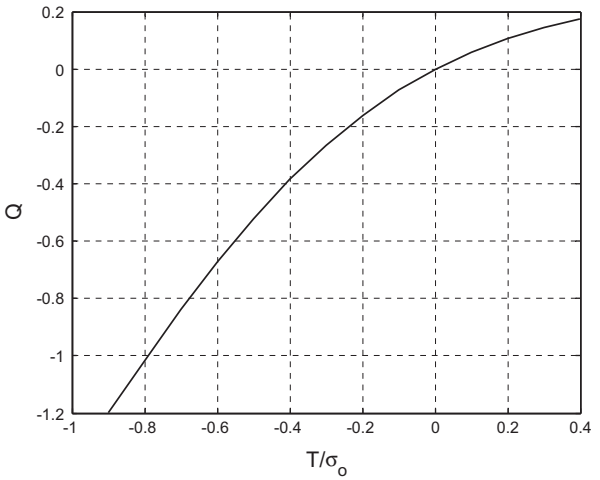

Fig. 3. Relationship between normalized T-stress and Q.

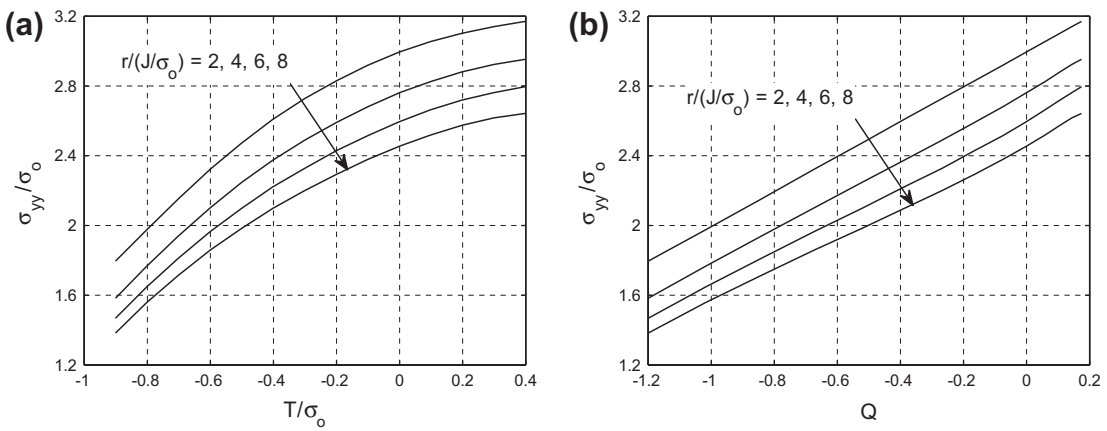

Fig. 4. Reference opening stress as a function of (a) T/σ_o and (b) Q for normalized radial distances $r/(J/\sigma_o) = 2$, 4, 6, and 8.

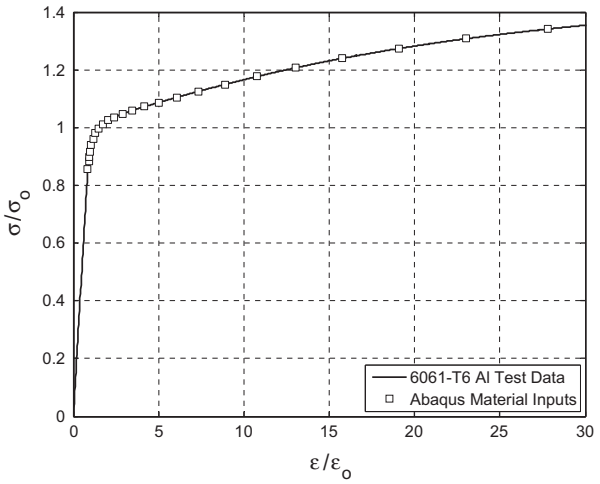

Fig. 5. 6061-T6 tensile test data and Abaqus inputs. The reference strain is defined as $\varepsilon_o = \sigma_o/E$.

discretized Abaqus inputs are shown in Fig. 5, as a solid line and hollow points respectively. Incremental theory plasticity, which follows the von Mises yield criterion (J_2 flow rule), is used for this analysis.

A COPV overwrap consists of multiple overlapping carbon fiber epoxy layers filament wound at different angles relative to the vessels axis comprising the layup. In order to define the elastic nature of the overwrap, only material constants defining an orthotropic material are necessary. Assuming there is sufficient individual fiber windings for each layer defined by angle β and the filament wound process produces a symmetric layup; the resultant material definition can be approximated as a symmetric angle-ply laminate, essentially making an axisymmetric material model about the cylindrical axis [23]. Engineering constants for each angle-ply layer are calculated by transforming from the original properties ($\beta = 0^\circ$), where the wind angle β is defined from the cylindrical axis of the pressure vessel. Therefore, the longitudinal direction is at $\beta = 0^\circ$ and the hoop direction is at $\beta = 90^\circ$. The Abaqus Wound Composite Modeler 6.7–3 plug-in is used for the material calculations [22].

The material properties of the carbon fiber epoxy T700-24K-50C are used in the finite element analysis. This material is used in the sub-scale COPV fracture specimens tested for NASA. The elastic engineering constants for the T700-24K-50C carbon fiber epoxy material calculated based on 65% fiber volume normalized by the aluminum yield strength (σ_o) are as follows: $E_1/\sigma_o = 527$, $E_2/\sigma_o = E_3/\sigma_o = 78.9$, $\nu_{12} = \nu_{13} = 0.326$, $\nu_{23} = 0.514$, $G_{12}/\sigma_o = G_{13}/\sigma_o = 27.1$, $G_{23}/\sigma_o = 26.0$. Where E_1, E_2 and E_3 are the moduli in the fiber, transverse and thickness directions respectively, G_{ij} are the shear moduli and ν_{ij} are the Poisson's ratios.

3.2. Geometries and loads

Fig. 6 shows a surface crack from the sub-scale COPV test specimens. The initial laser notch was placed in the center of the cylindrical section such that the crack opened in the hoop direction. In order to simplify experimental techniques, this crack is located on the outer liner surface. Pre-cracking was done with cyclic pneumatic loading of the liner before wrapping. After wrapping, the test conditions consisted of a single over-pressure load to simulate autofrettage at 26.23 MPa (3804 psi) and 200 cycles at 16.96 MPa (2460 psi) to simulate operational life. During manufacturing, the autofrettage load is applied to compensate for thermal strains induced from curing by joining the liner to the overwrap with residual compressive stresses from plastic deformation. The initial and final crack fronts are shown in Fig. 6. The pre-cracks in the COPV specimens did not produce a through flaw during cyclic loading and crack growth from the outer surface was minimal. For purposes of finite element analysis, a crack opening on the interior liner surface is of greater interest, see Fig. 7. This placement is considered more critical in terms of crack mouth opening because crack opening is directly restricted by the overwrap for a crack located on the outer liner surface. Crack growth is not directly modeled in this study; therefore, these experimental results will only serve as a base to compare the global material response of our finite element models.

The sub-scale COPV specimen was designed to achieve an autofrettage and maximum operating pressure to ensure plasticity in the liner without burst. Due to the small cylindrical radius, the relative thickness of the applied overwrap is not typical. The overwrap to liner thickness ratio would typically be higher ($t_{Wrap} \approx 3t_{Liner}$). Nevertheless, the effects of the overwrap on near tip fields should still be quantifiable.

Fig. 8 gives the average hoop and longitudinal surface strain data taken from eight gages (four gages oriented in the hoop direction and four in the longitudinal) adhered to the outer surface of the overwrap of an uncracked sub-scale COPV specimen at the center of the cylindrical section separated by 90° about the cylindrical axis. This specimen is identical to the initial COPV geometries before laser notching. This data will be simulated using a 3D finite element model to be described in a later section. The inability to acquire crack mouth opening data from this specimen inherently leads to inaccuracies in near

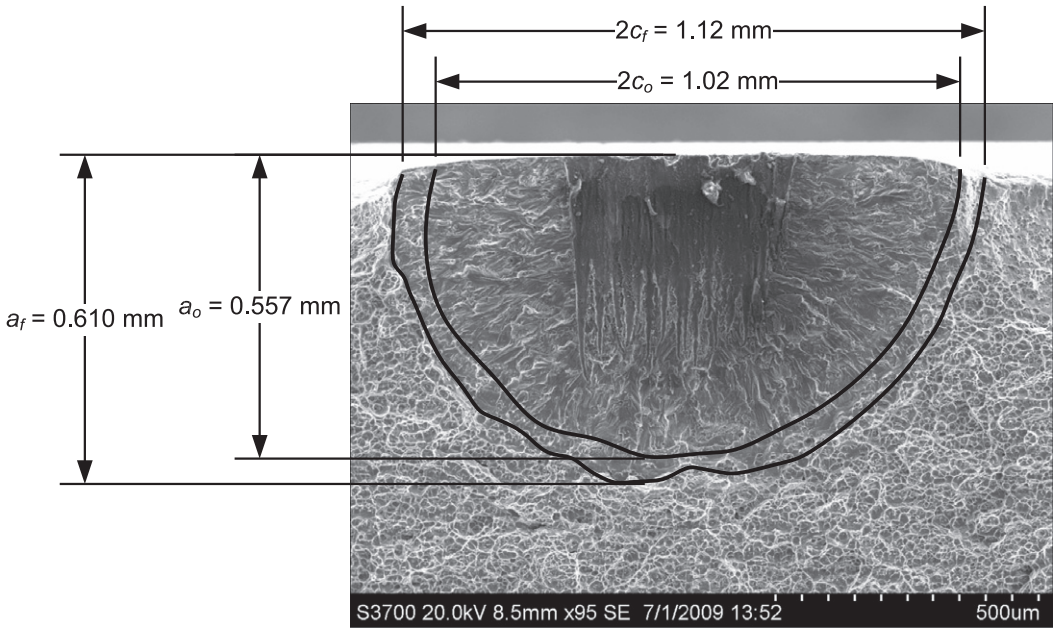

Fig. 6. Surface crack from sub-scale COPV.

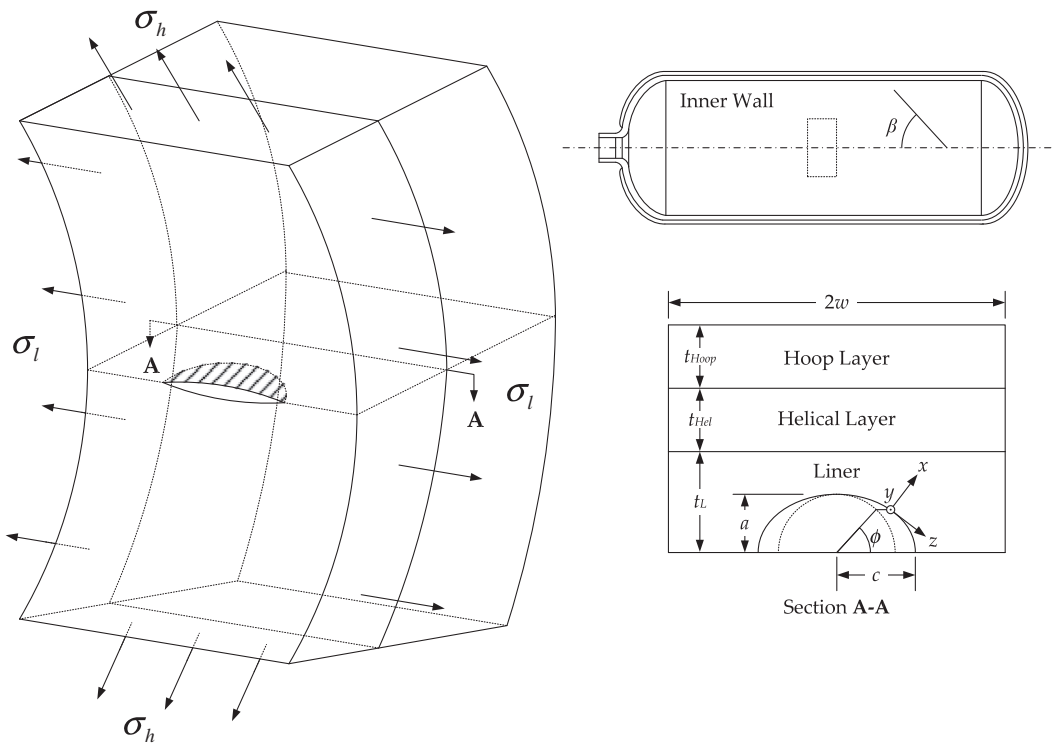

Fig. 7. Schematic of the surface crack section from a COPV liner. A local coordinate system is applied to the crack front. Far field loads are defined for the pressure vessel as hoop (h) and longitudinal (l) directions with the hoop and y directions coinciding at the crack plane.

tip measurements [12], but the high accuracy in outer strain data provides confidence in the numerical estimations. The geometry, materials, and loads will be used in preliminary analyses before implementing additional COPV geometries. In this study, two liner and COPV geometries are implemented; a sub-scale, matching the dimensions and loads described above and a full-scale, in which typical COPV dimensions are used. The full-scale COPV, with a three to one overwrap to liner

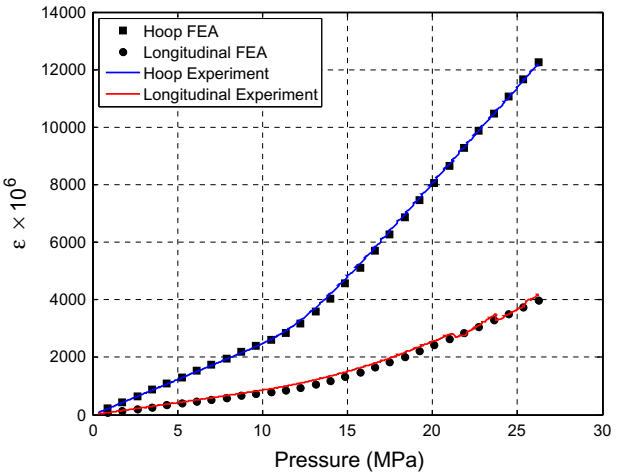

Fig. 8. Strain data from the sub-scale COPV specimen and 3D FEA results.

thickness ratio ($t_{Wrap} \approx 3t_{Liner}$), is similar to those typically used in aerospace applications. Liner only models (homogeneous pressure vessels) are studied as a basis for comparison. Tables 1 and 2 provide the dimensions for the global liner and COPV models respectively.

Two semicircular crack sizes are inserted into each of the sub and full-scale liners. The sub-scale liner contains a crack with $a/t = 0.267$ corresponding to the maximum depth shown in Fig. 6 and $a/t = 0.5$ implemented to assess the effects of greater crack penetration. The full-scale liner contains cracks of $a/t = 0.5$ and 0.7. The later depth ratio is typical for minimum detectable crack sizes for various non-destructive evaluation (NDE) techniques.

A global finite element model is implemented for each of the four geometries tested. Semicircular cracks of various depths are inserted in a sub-model section of the liners at the center of the cylindrical portion. The longitudinal and hoop edge lengths of this section are 38.1 × 38.1 mm. Fig. 7 is a schematic representation of the liner model with the crack section description and placement. Quarter symmetry boundary conditions are placed at half the axial length and the half-circle cylindrical cross section, such that only a quarter of the crack face placed at the center of the cylindrical section opening in the hoop direction is modeled. A typical single inlet COPV is not strictly quarter symmetric. However, the crack is assumed sufficiently far from end caps to be unaffected by the different geometries (inlet or dome). Only the quarter containing the inlet is modeled for the global COPVs. Sub-model boundary conditions are then used to apply displacements to the cracked models. COPV sub-models are implemented complete with anisotropic overwrap from the cut section of the global COPV. Greater mesh density is given to the region of the overwrap section opposite the liner crack. A finite thickness adhesive layer is generally present between the overwrap and the liner. However, the layer thickness is small compared to overwrap and liner dimensions; therefore, it is ignored for this analysis. The COPV models use Abaqus tie constraints to "adhere" the metallic liner to the composite overwrap. A tie constraint couples the nodal displacements of the slave surface, in this case the liner, to the displacement field of the master surface (overwrap). Therefore, the model assumes a perfect bond with zero adhesive thickness. Pressure loads are applied to the global and sub-model inner surfaces using distributed loads.

A simulation of the autofrettage load at 26.23 MPa (3804 psi) is applied to the sub-scale COPV model. The maximum expected operating pressure (MEOP) of 16.96 MPa (2460 psi) is isolated for analysis before autofrettage load is achieved. The residual stresses and strain-hardening effects cause by autofrettage will be ignored for the MEOP cycle. A MEOP load of

Table 1
Dimensions of the metallic liner models.

Model	Material	t_L (mm)	d_i (mm)	L (mm)
Sub-liner	6061-T6 Al	2.29	157	504
Full-liner	6061-T6 Al	1.27	498	1149

Table 2
Dimensions of the COPV models.

Model	Liner	Material	t_{Hel}, β (mm, Deg)	t_{Hoop}, β (mm, Deg)
Sub-COPV	Sub-liner	T700-24K-50C	0.665, 12.2°	0.686, 90°
Full-COPV	Full-liner	T700-24K-50C	1.91, 11.8°	1.91, 90°

20.68 MPa (3000 psi) is applied to the full-scale COPV model. This load provides sufficient liner plasticity for this analysis; therefore, an autofrettage load will not be applied. Pressures of 8.76 MPa (1271 psi) and 1.671 MPa (242.9 psi) are applied to the liner sub-scale and full-scale liner only models respectively, to achieve a nominal equivalent (von-Mises) stress approximately equal to the their respective COPV liner load at MEOP.

3.3. Finite element mesh

FEA Crack version 3.1.14 [24] was used to generate the crack mesh in the cut liner section and Abaqus version 6.7 [22] was used for the global and sub-model analysis. The *J*-integrals along the crack front are calculated using the domain integral method intrinsic to Abaqus. The finite element analyses are made using C3D20R 20-node isoparametric brick elements. At the crack-tip, 20-node collapsed face prismatic elements are used. To allow for crack tip blunting in the elastic–plastic models, the initially coincident nodes at the crack tip are left unconstrained. A highly refined near tip mesh consisting of 31 contours around the crack tip and 72 collapsed face elements along the crack front is used to ensure sufficient radial points for stress field analysis. Fig. 9 shows the sub-model crack mesh with these refinements.

A study of mesh refinement was conducted by comparing domain integral measurements (*J*-integral), which tend to be sensitive to mesh refinement, from various models of mesh density. With increasing mesh refinement, the mean *J*-integrals at each crack angle ($J(\phi)$), calculated by averaging the values from the outer most contours (20–30) in which the *J*-integral varied by a negligible amount (<0.50%), converged to stable values and continued through the mesh refinement used for this analysis. The chosen mesh refinement is beyond the level needed for accurate stress and domain integral calculations, but was necessary to achieve sufficient radial data points to assess stress fields. A study was completed to determine the accuracy of the final mesh configuration compared to a coarser but still convergent mesh. The near tip stress measurements obtained by a less refined mesh compared accurately to the results from the final mesh refinement when the number of radial points in the coarse mesh used in interpolation is maximize by limiting range of deformations observed. The finer mesh was necessary to analyze deformation dependent radial distances for a wide range of loads.

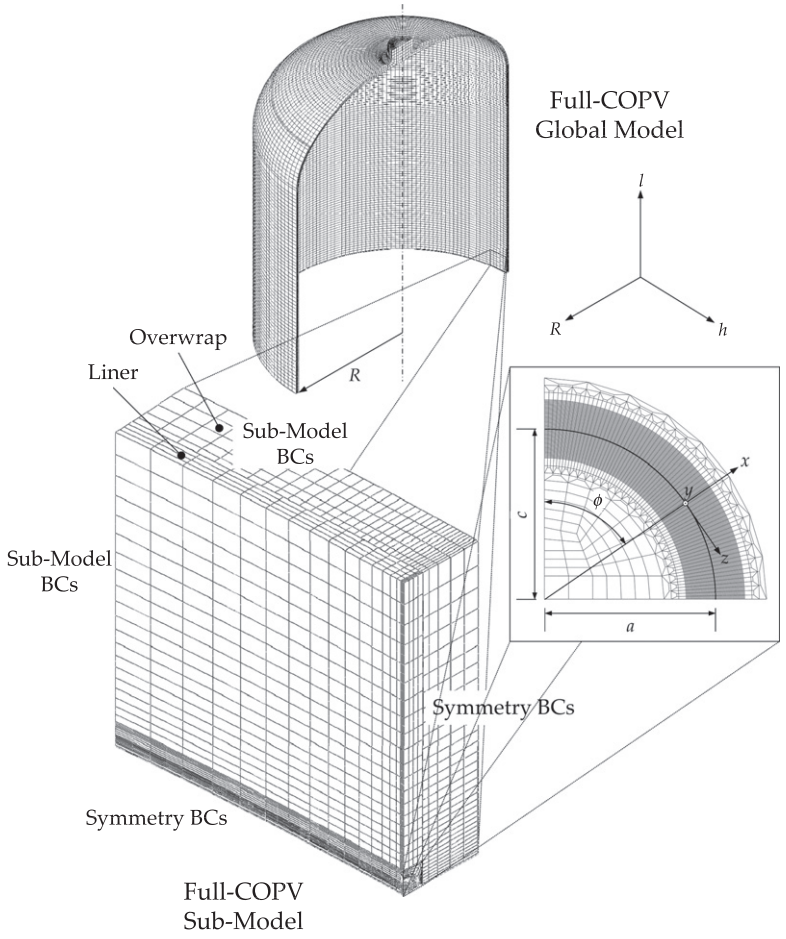

Fig. 9. FEA visualization of the surface cracked liner sub-model. Far field loads are defined for the pressure vessel as hoop (*h*), longitudinal (l) and radial (*R*).

Crack tip blunting effects can typically be neglected at distances roughly twice the crack-tip opening displacement or $2J/\sigma_o$. Inside this distance from the crack tip, it would be necessary to use large strain analysis [25]. For this investigation, small strain approximation will be used to analyze stress fields outside the crack-tip blunting zone.

4. Results and discussion

4.1. J–Q and critical crack angle

Figs. 10 and 11 show the J-integral (a) and Q (b) as a function of crack angle ϕ at a constant nominal equivalent stress $\sigma_\infty = \sigma_o$ for the sub-scale (Fig. 10) and full-scale (Fig. 11) models. The deeper cracks consistently show greater normalized J values even when normalized by crack depth. Similarly, due to the differences in strain distribution on the bonded surface caused by the continued partial elasticity of the structure, the overwrapped geometries (COPV) show significant reduction in J when compared to all the homogeneous geometries (liner only), for both deep and shallow cracks. This indicates that the relative local deformation, measured as the ratio of J to relevant specimen dimensions, is significantly higher in deeper cracks and geometries without overwrap. Since this effect is a similar function of both overwrap and relative crack depth, the overwrap essentially increases the effective thickness of the geometry from a fracture standpoint.

The uniaxial bonded structure investigated in the previous work [1], demonstrated a strong influence of the elastic backing on T-stress constraint measurement. The greatest effect was shown at crack depth, where the in-plane stress acting in the T direction was directly influenced by the dimpling resistance caused by the backing, where dimpling is defined as displacement normal to the plate on the face opposite crack opening. This study cannot be entirely applied to a biaxial structure with Q as the constraint measurement. Figs. 10b and 11b show the strong increase in Q near the free surface caused by the biaxial component of stress (longitudinal stress). In addition, since Q is measured here under large-scale yielding

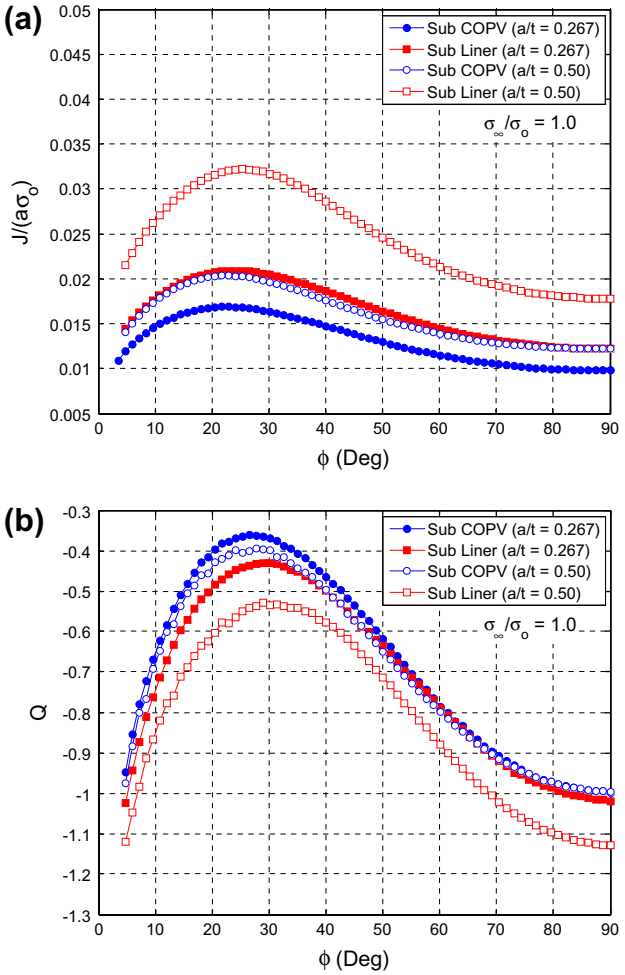

Fig. 10. (a) J and (b) Q crack front distributions for the sub-scale COPV and liner models at a nominal equivalent stress $\sigma_\infty = \sigma_o$.

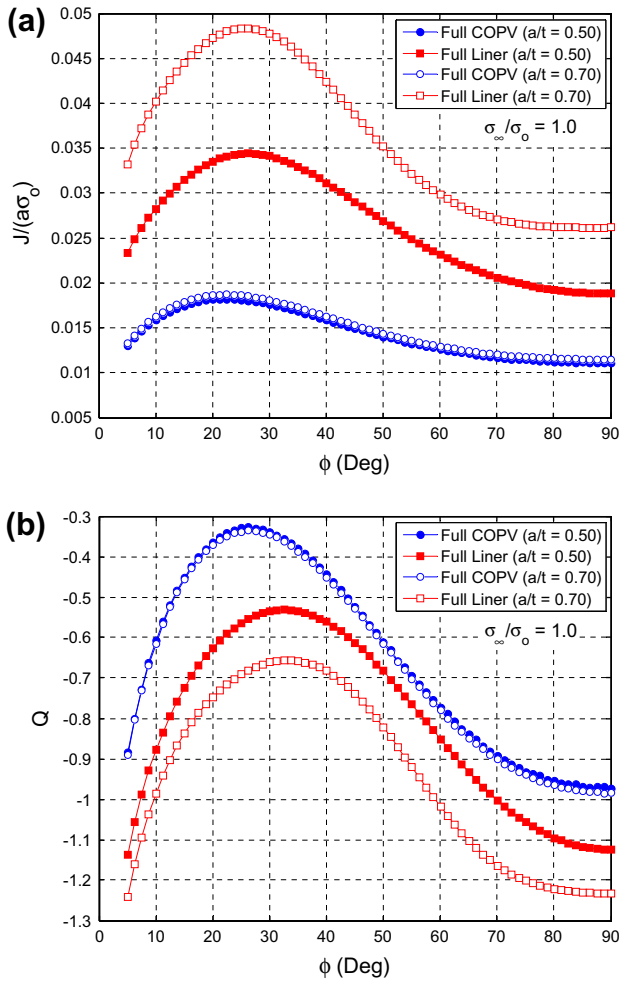

Fig. 11. (a) J and (b) Q crack front distributions for the full-scale COPV and liner models at a nominal equivalent stress $\sigma_\infty = \sigma_o$.

conditions, the correlation of Q and elastically scaled T cannot be assured. Nevertheless, some similarities exist in Q measured here and the elastic T-stress from the uniaxial case. The Q values computed in the COPV geometries are greater compared to liner only geometries, with the greatest differences found at crack depth, caused by the overwrap, and near the angle of maximum Q, caused by differences in the biaxial ratio. The existence of the overwrap often decreases the ratio of hoop stress to longitudinal stress (biaxial ratio) compared to homogeneous pressure vessels resulting in a higher longitudinal component. The shallow crack in the sub-COPV does not demonstrate any significant effect of the overwrap at crack depth because the crack is sufficiently far from the bonded layer.

Crack depth has only a minor effect on Q measured in the COPV geometries, indicating the increased effective thickness caused by the overwrap is sufficient to maintain a value of Q unaffected by small increases in crack depth. However, crack depth in the homogeneous geometries has a significant effect of Q, with deeper cracks showing greater constraint loss (lower Q) for a given nominal load.

The presence of the overwrap also has a small effect of the angle of maximum J and Q values. In both cases, the maximum is found at an angle closer to the free surface in the COPV geometries.

Observing the peaks of both J and Q given in Figs. 10 and 11, the product of the J-integral and opening stress (σ_{yy}) at a radial distance ($r = 2J/\sigma_o$) as a function of crack angle ϕ for $\sigma_\infty = \sigma_o$ in the sub-scale and full-scale models can be estimated. The opening stress (σ_{yy}) at a radial distance ($r = 2J/\sigma_o$) is simply used to determine the level of constraint that is not dependent on the SSY solution, shown in Fig. 2. Therefore, the product of J and $\sigma_{yy}(r = 2J/\sigma_o)$ can be used in a similar manner to Leach et al. [26] to predict the critical crack growth angle. Assuming radial independence of Q, this methodology should produce relatively accurate critical crack growth angles. The assumption that the opening stress distribution will produce a radially independent measure of Q is shown to be invalid as the collapse or over relaxation of near tip fields is no longer represented by the J–Q MBL predicted state. Consequently, the shape of this curve is moderately influenced by load and the actual crack growth mechanism may or may not be controlled by J and Q. Therefore, the critical crack growth angles

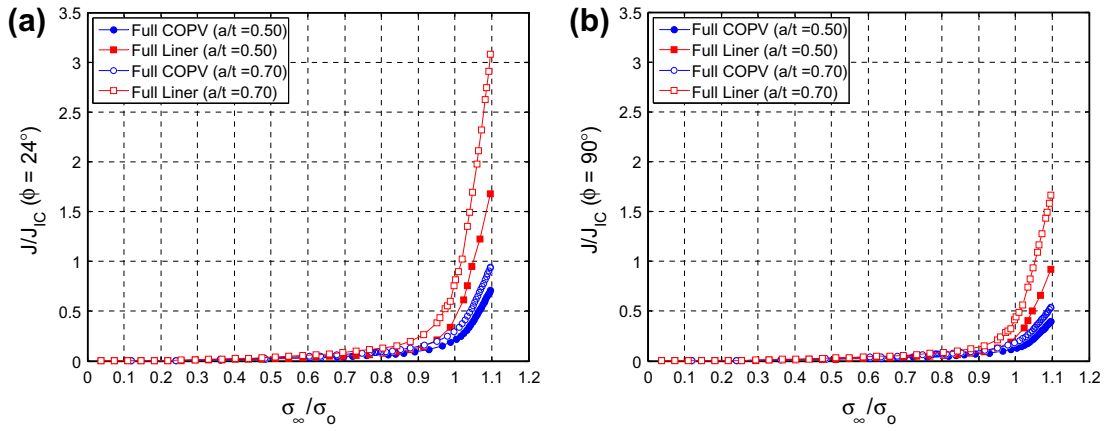

Fig. 12. J normalized by J_{IC} as a function of nominal equivalent liner stress (σ_∞) for angles $\phi = 24°$ (a) and 90° (b) in the full-scale COPV and liner models.

taken from this methodology, where the actual crack extension load is not known, should only be taken as an engineering approximation. The angle of interest corresponding to the COPV maxima is $\phi = 24°$. The crack angle of $\phi = 90°$ will also be analyzed in subsequent sections because growth in the crack depth direction is critical in terms of developing a through crack in the liner. A clear shift towards crack depth occurs in the liner only models. This corresponds to the angular shift towards crack depth in both maximum J and Q shown in Figs. 10 and 11. For simplicity, comparisons will only be made at angles $\phi = 24°$ and 90° in both the COPV and liner only models.

Typically, crack-tip opening displacement (CTOD) and driving force (J-integral) measurements are taken from FEA coupon or structure models to compare with critical values. For two-parameter fracture prediction, this is done with a failure locus as a function of constraint, where lower constraint yields higher toughness or resistance to crack growth. A conservative comparison between measured J and a critical J can be made with elastic plane strain fracture toughness (K_{IC}) of 6061-T6 aluminum converted to J_{IC} using Eq. (5). This value does not account for the increases in apparent fracture toughness with constraint loss and strain energy dissipation associated with plastic strains near the crack tip and therefore is not necessarily associated with critical crack growth. Fig. 12a and b give J normalized by a critical value for angles $\phi = 24°$ and 90° in the full-scale models as a function of nominal equivalent stress in the liner (σ_∞/σ_o). The critical J-integral (J_{IC}) from plane strain fracture toughness K_{IC} used to normalize Fig. 12 is $J_{IC} = 14.22$ kPa m [27]. These figures are shown only to the maximum load shared in each group, $\sigma_\infty = 1.10\sigma_o$ for the full-scale models.

By looking only at the driving force and ignoring constraint/triaxial effects on apparent toughness, the overwrap in a COPV significantly increases the resistance to crack failure as a function of load. Both the sub-scale and full-scale models show this trend in loading trajectory. However, the full-scale model shown here, with its higher overwrap to liner thickness ratio, experiences a stronger effect of the overwrap compared to the sub-scale model of equivalent crack penetration ($a/t = 0.50$).

4.2. Near tip field characterization limits

Two general conclusions can be made by comparing near tip fields to J–Q MBL predicted fields. Firstly, the adherence of near tip fields at a radial distance of $r = 4J/\sigma_o$ indicates how the level of far-field loads and crack tip deformations affect the near tip opening fields compared to a J–Q prediction, providing a simple and clear measure of J–Q dominance. Secondly, because Q, as defined in MBL formulation (Eq. (2)), is an offset measure of opening stress at $r = 2J/\sigma_o$, a comparison at a greater radial distance, here $r = 4J/\sigma_o$, provides a relative measure of radial independence of Q. The accurate prediction of stress fields in this range, where both cleavage and ductile fracture mechanisms are present, provides a valid engineering measure of J–Q dominance. Note that the ductile fracture mechanism is most prevalent in crack growth for aluminum alloys.

The most obvious and significant comparison with regard to the fracture driving force is of the opening stresses (σ_{yy}) in the crack plane ($\theta = 0°$) as functions of nominal load and near tip deformation. Engineering geometric standards for crack specimens use a factor that is directly proportional to relevant specimen dimensions and inversely proportional to crack driving force to specify minimum dimensional requirements in order to ensure a size-independent measure of toughness. Therefore, the local deformation factor $a\sigma_o/J$ is an inverse measure of local deformation and can be used as a relative measure of specimen characteristic length requirements.

The opening stress (σ_{yy}) normalized by J–Q MBL predicted stress at $r = 4J/\sigma_o$ as a function of nominal equivalent liner stress σ_∞ and local deformation factor $a\sigma_o/J$ is investigated at $\phi = 24°$ and 90° in all the geometries tested. In some cases, the homogeneous deep cracks at angles near crack depth produced Q values that were lower than the extent of MBL predictions; Q is therefore not extrapolated and these points are typically omitted. These trends will be analyzed in the subsequent section when Q is given as a function of load.

Previous work demonstrated that the allowable far-field load before field collapse, designated by a greater than 5% difference from J–T MBL solutions, is greater for bonded geometries [1]. It was also found in a follow-up study that for these uniaxial geometries, the allowable local deformation was significantly greater at crack depth for the bonded case; however, in the region of maximum J ($\phi \approx 24^\circ$) the unbonded geometries produced slightly higher allowable deformations before J–T collapse. J–Q analysis of the biaxial fields in the pressure vessel geometries produces similar results.

The sub-scale and full-scale models produce nearly identical trends. Although some differences exist for the near tip fields at crack depth ($\phi = 90^\circ$), the general trends in the data do not seem to demonstrate a clear effect of the overwrap at this angle. However, the fields remain within 5% of the MBL solutions for the loads tested. Therefore, the fields are said to maintain J–Q dominance for the loads and deformations at $\phi = 90^\circ$ and radial distances $2J/\sigma_o \leqslant r \leqslant 4J/\sigma_o$. A clearer picture of near tip trends and plastic collapse can be observed for the angle in the critical region ($\phi = 24^\circ$).

Table 3 gives the values of nominal equivalent liner stress and corresponding local deformation factors for $\phi = 24^\circ$ at the points of 5% deviation ($\sigma_{yy}/\sigma_{MBL} = 0.95$) in the MBL normalized opening stress field. As shown in the studies discussed above, the allowable nominal stresses and local deformation factors are higher (higher stress and smaller deformation) for the COPV models. This indicates that the increased resistance to crack opening caused by the overwrap dominates the near tip field's resistance to plastic collapse. This results in high stresses with limited crack opening at the point of field collapse.

4.3. Constraint loss and triaxiality in the full-scale COPV

The results from both the sub-scale and full-scale models have shown similar trends in J, Q and near tip stress field measurements. In addition, the trends observed in the full-scale model are stronger and therefore more helpful in drawing conclusions from the results. The following sections deal only with the full-scale COPV.

Fully elastic models are used to calculate T-stress scaling factors, which are normalized by the nominal hoop stress (σ_h) of the liner. Fig. 13 gives these factors for the full-scale COPV and liner geometries. The elastic biaxial ratio (hoop over longitudinal stress) is significantly different in the wrapped verses un-wrapped geometries. Nominal hoop verses longitudinal stress in the liner is 2.0 without overwrap and 1.6 with overwrap. The higher longitudinal stresses in the COPV account for the increase in T-stress at lower crack angles. Stresses acting in the crack plane are added to the T-stress. In this case, the longitudinal stress is added to the T-stress as a cosine function of crack angle. At crack depth, where no biaxial effects are present, the deep crack has a slightly higher T-stress in the COPV compared to the liner only model. While this difference is not noticeable for $a/t = 0.50$, the deeper crack shows greater tensile stresses generated by the overwrap stiffness.

The MBL generated Q verses T-stress curve, shown in Fig. 3, is the difference in the J–T predicted opening stress and the SSY solution at $r = 2J/\sigma_o$. Therefore, comparing Q and Q predicted from T or $Q(T)$ as a function of load is essentially the comparison of J–Q and J–T opening stress fields. With increasing load and the onset of large-scale yielding, near tip stresses will drop nonlinearly for low constraint geometries. Additionally, as plastic flow proceeds through the remaining ligament, T-stress loses its meaning as a constraint parameter and Q deviates significantly from $Q(T)$. Figs. 14 and 15 give Q and $Q(T)$ as a function of local deformation $a\sigma_o/J$ and nominal equivalent stress σ_∞ respectively.

Large-scale yielding occurs when the near tip stress conditions deviate significantly from the elastic solution. The existence of a K scaled asymptotic field is not assured. The ratio of elastic–plastic J to elastic J_{EL} estimate using Eq. (5) and a linearly scalable K_I, can be used to determine the onset of large-scale yielding. An arbitrary limit of 10% deviation is placed on this ratio and the corresponding loads are given in Table 4 for the full-scale models.

Therefore, Figs. 14 and 15 primarily show only loads after the onset of large-scale yielding and up to and including plastic collapse. Even under biaxial stresses Q remains relatively close to $Q(T)$, prior to the onset of large-scale yielding. However, the near surface ($\phi = 24^\circ$) curves significantly deviate after this point.

At crack angle $\phi = 24^\circ$, the increase in crack penetration ($a/t = 0.50 \rightarrow 0.70$) in both global geometries does not have a significant effect on Q. Conversely, increased crack penetration results in a more rapid decrease in Q for larger loads and deformations at $\phi = 90^\circ$ in the liner geometry. As plastic flow progresses through the remaining ligament at crack depth, stress field relaxation is a result of loss of near tip triaxiality. This effect is enhanced with the decrease in remaining ligament. Interestingly, this same phenomenon has the opposite effect in the COPV geometry. The increase in crack depth results in the fields being measured at a distance closer to the bonded surface for $\phi = 90^\circ$, resulting in higher constraint values for larger

Table 3
J–Q dominance limit loads at $\phi = 24^\circ$.

Model	a/t	$a\sigma_o/J$	σ_∞/σ_o
Sub-COPV	0.267	71.4	0.985
Sub-liner	0.267	64.7	0.980
Sub-COPV	0.50	73.4	0.964
Sub-liner	0.50	65.9	0.951
Full-COPV	0.50	73.5	0.971
Full-liner	0.50	64.0	0.938
Full-COPV	0.70	72.1	0.966
Full-liner	0.70	63.9	0.911

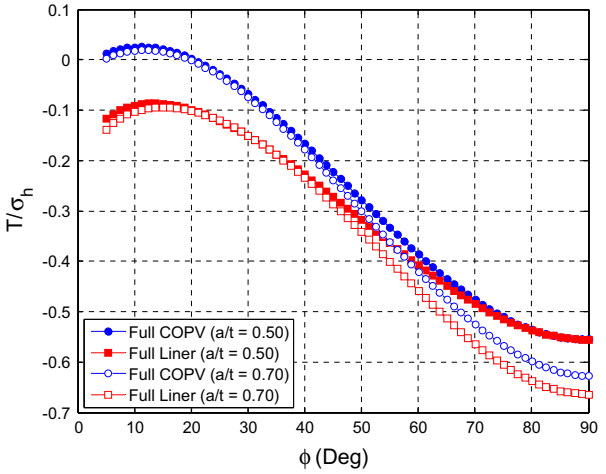

Fig. 13. T-stress scaling factors (T/σ_h).

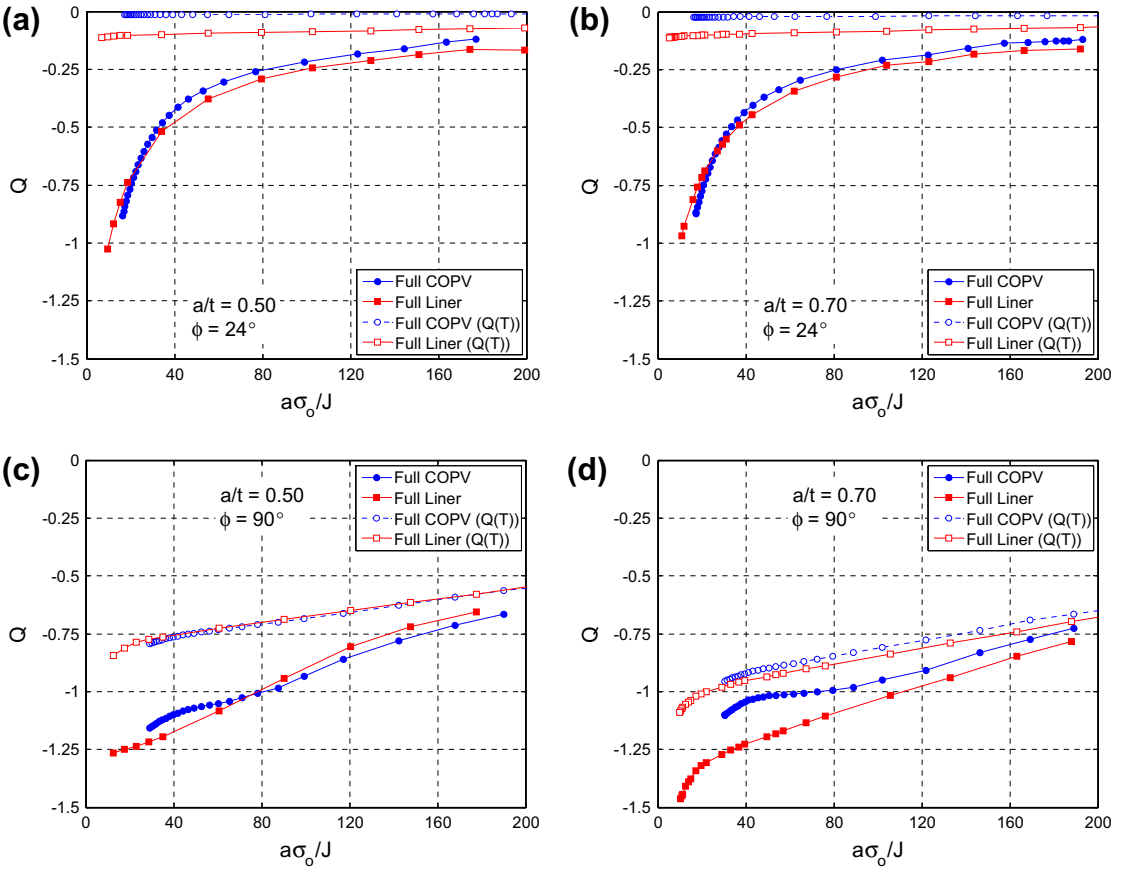

Fig. 14. Q and $Q(T)$ as a function of local deformation $a\sigma_o/J$.

deformations compared to the shallower crack. Because MBL formulations rely on high triaxiality (plane-strain), the Q maintains a closer relationship to $Q(T)$ at large loads for the deeper crack.

At crack depth, Q maintains approximately a linear relationship with load up to very large deformations making $Q(T)$ a more accurate approximation. However, for both angles tested Q deviates significantly from $Q(T)$ at larger loads. The general

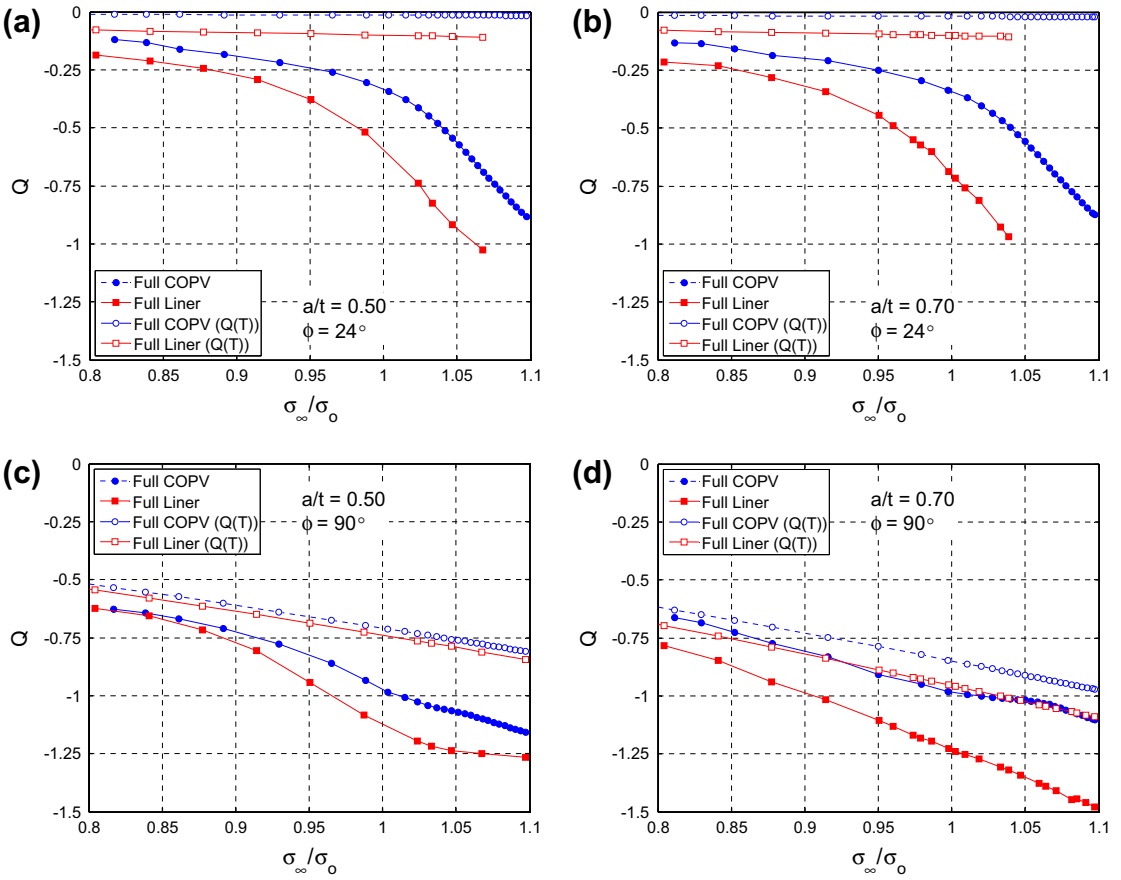

Fig. 15. Q and $Q(T)$ as a function nominal equivalent stress σ_∞.

Table 4
Points of large-scale yielding ($J/J_{EL} = 1.10$).

Model	a/t	ϕ	$a\sigma_o/J$	σ_∞/σ_o
Full-liner	0.50	24°	186	0.750
Full-COPV	0.50	24°	176	0.820
Full-liner	0.50	90°	174	0.847
Full-COPV	0.50	90°	174	0.883
Full-liner	0.70	24°	219	0.661
Full-COPV	0.70	24°	177	0.798
Full-liner	0.70	90°	197	0.792
Full-COPV	0.70	90°	173	0.872

conclusion is that T fails to predict accurate stress fields for moderate levels of deformation and nominal equivalent stress levels in a biaxial configuration.

Ductile fracture occurs by void-nucleation, growth and coalescence in metals [28–31]. Near tip triaxiality, defined as the ratio of hydrostatic stress to von-Mises stress, directly controls void-nucleation and growth, therefore a constraint parameter should accurately represent triaxiality. Henry and Luxmoore [8] in their study on the relationship between triaxiality and Q for low constraint geometries, indicate that there is a unique linear relationship between Q, measured at $r = 2J/\sigma_o$, and triaxiality. This relationship is independent of geometry and level of deformation. Therefore, one would expect the near tip triaxiality to maintain a linear relationship with Q for the homogeneous (liner-only) models for all levels of deformation tested. This is not necessarily true for the COPV models, because the material is discontinuous through the thickness. The ratio of mean stress to von-Mises stress is given by:

$$\frac{\sigma_m}{\sigma_e} = \frac{\sqrt{2}(\sigma_1 + \sigma_2 + \sigma_3)}{3\sqrt{(\sigma_1 - \sigma_2)^2 + (\sigma_2 - \sigma_3)^2 + (\sigma_1 - \sigma_3)^2}} \tag{6}$$

where σ_1, σ_2, and σ_3 are the principal stresses.

Figs. 16a and b give the ratio of mean stress to von-Mises stress verses Q at a radial distance $r = 2J/\sigma_o$ for the full liner and COPV models at angles $\phi = 24°$ and 90° respectively. In the liner only models, for the near surface angle ($\phi = 24°$), the triaxiality is lower for a given value of Q compared to those measured at crack depth ($\phi = 90°$), indicating that the relationship between triaxiality and constraint loss is weakly affected by the addition of a biaxial stress. Nevertheless, triaxiality and Q maintain a linear relationship that is a moderate function of ϕ.

If deformation levels and geometry facilitate a hydrostatic shift in stress fields measured by Q, opening stress must inherently agree with J–Q predictions in the process zone. However, out-of-plane and hydrostatic stress components may determine whether the trends in Q maintain a linear relationship with triaxiality, which is desirable for Q as a ductile fracture parameter.

It is important to indicate the level of Q experienced when plasticity prevails over the entire cylindrical portion of the liner in order to evaluate trends. For the angles $\phi = 24°$ and 90°, Q measured at a nominal equivalent stress of yield ($\sigma_\infty = \sigma_o$) can be estimated in Fig 11b for the full-scale model.

Triaxiality more or less maintains an equivalent relationship to Q for a given angle up to the region of nominal (far-field) yield. When this load is exceeded, the triaxiality as a function of Q increases in the COPVs compared to the liner only, which maintains linearity through the loads shown. Except for the deep crack ($a/t = 0.70$) at crack depth ($\phi = 90°$), the increased trend in the COPV models is gradual. However, an increase in triaxiality with a decrease in Q is seen for a small region corresponding with nominal yield for the deep crack ($a/t = 0.70$) at crack depth ($\phi = 90°$) in the COPV model. In this region, Q remains relatively unchanged (Fig. 15d), while the far-field load and therefore J and triaxiality continue to increase. The increase in near tip triaxiality and radial distance of measure (linear with J), results in a stronger dependency of the bonded relationship. Correspondingly, all bonded geometries demonstrate a greater influence on the material discontinuity for loads

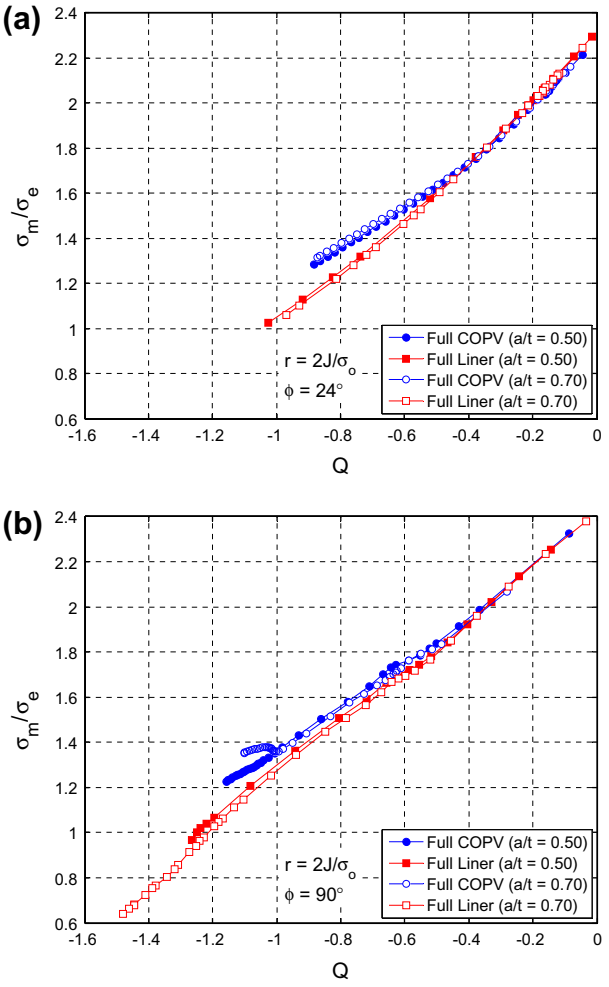

Fig. 16. The ratio of mean stress to von-Mises stress at a radial distance $r = 2J/\sigma_o$ verses Q for the full liner and COPV models at angles $\phi = 24°$ (a) and 90° (b).

causing full-scale yielding. Essentially, the continued elasticity in the structure maintains higher levels of stress for loads causing yield in the liner portion.

5. Conclusions

Fracture characterization in geometries where loads exceed net-section yield is difficult and requires a thorough analysis of the near tip fields. The COPV geometry further complicates the analysis because of its material discontinuity and anisotropy. An engineering approach to the parameterization of surface cracks in COPV liners is given, both from a deformation limit and conservativeness perspective. J and Q crack front distributions, and the corresponding limits, and near tip triaxiality and constraint loss trends are obtained and the effects of elastic–plastic material discontinuity of the COPV and the biaxiality of stresses are evaluated. The following conclusions are summarized:

(1) Crack mouth opening and subsequent near tip crack intensity (J-integral) is significantly reduced as a function of far-field load with the addition of the overwrap. Therefore, from a perspective of single parameter fracture prediction, COPVs cannot be treated as a homogeneous structure. Incorporating the overwrap in fracture measurements will achieve a more adjusted and less conservative estimate of failure.
(2) J–Q predicted fields maintain accuracy (Q is radially independent) for higher far-field loads and lower near tip deformations compared to the liner only models for angles near the free surface. This indicates that the resistance to crack opening (lower near tip deformations) outweighs the effects of near tip field relaxation in the COPV geometry at these angles.
(3) J–Q fracture prediction of surface cracks in COPV metallic liners is possible up to large deformations. However, for the critical crack growth region ($\phi \approx 24^\circ$) in a semicircular crack, Q does not maintain a radially independent measure of constraint for loads seen in a typical COPV; therefore, these fracture predictors may not be applicable.
(4) The triaxiality and Q relationship becomes non-linear with large deformations for the COPV models, while homogeneous models maintain a linear relationship independent of deformation. At crack depth for the deeply crack full-scale COPV, where the influence of the overwrap is most prevalent, large-scale yielding marks a transition where triaxiality increases with loss of constraint. As a ductile fracture parameter, Q is to maintain a linear relationship with triaxiality; therefore, this effect will have consequences on the prediction of ductile crack growth.
(5) The trends in near tip stress fields referenced to MBL solutions seen in the COPV geometries are similar to uniaxial cases studied in the part I paper. The Q from elastic T-stress ($Q(T)$) maintains relatively accurate predictions of Q for crack depth angles where the overwrap has the greatest effect, indicating J–T fields are accurate in this region. However, the addition of the biaxial stress drastically reduces J–T predictability for angles near the free surface.

Acknowledgements

The authors express their appreciation for the support provided by the NASA Marshall Space Flight Center (MSFC). Ongoing, unpublished research at MSFC concerning the deformation limits for surface crack testing laid the foundation for many of the analytical tools and techniques used in this study. The authors also thank the NASA Langley Research Center (LARC) for providing us with specimen data.

References

[1] English S, Arakere NK, Allen PA. J–T characterized stress fields of surface cracked metallic liners bonded to a structural backing-I. Uniaxial tension. Engng Fract Mech 2010;77:170–81.
[2] Newman JC, Bigelow CA, Shivakumar KN. Three-dimensional elastic-plastic finite-element analyses of constraint variations in cracked bodies. Engng Fract Mech 1993;46:1–13.
[3] Wang YY. On the two-parameter characterization of elastic-plastic crack-front fields in surface-cracked plates. Constraint Effects in Fracture ASTM STP 1993;1171:120–38.
[4] Wang YY, Parks DM. Limits of J–T characterization of elastic-plastic crack-tip fields. Constraint Effects in Fracture Theory and Applications: Second Volume ASTM STP 1995;1244:43–67.
[5] O'Dowd NP, Shih CF. Family of crack-tip characterized by a triaxiality parameter—I. Structure of fields. J Mech Phys Solids 1991;39:989–1015.
[6] O'Dowd NP, Shih CF. Family of crack-tip characterized by a triaxiality parameter—II. Fracture applications. J Mech Phys Solids 1992;40:939–63.
[7] Wang X. Two-parameter characterization of elastic-plastic crack front fields: surface cracked plates under tensile loading. Engng Fract Mech 2009;76:958–82.
[8] Henry BS, Luxmoore AR. The stress triaxiality constraint and the Q-value as a ductile fracture parameter. Engng Fract Mech 1997;57:375–90.
[9] Kikuchi M. A study on three-dimensional crack tip fields. Int J Pres Ves Piping 1995;63:315–26.
[10] Cicero S, Ainsworth RA, Gutiérrez-Solana F. Engineering approaches for the assessment of low constraint fracture conditions: a critical review. Engng Fract Mech 2010;77:1360–74.
[11] Silva LAL, Cravero S, Ruggieri C. Correlation of fracture behavior in high pressure pipelines with axial flaws using constraint designed test specimens. Part II: 3-D effects on constraint. Engng Fract Mech 2006;73:2123–38.
[12] Faleskog J. Effects of local constraint along three-dimensional crack fronts–a numerical and experimental investigation. J Mech Phys Solids 1995;43:447–93.
[13] Chao YJ, Zhu XK. Constraint-modified J–R curves and its application to ductile crack growth. Int J Fract 2000;106:135–60.
[14] MacLennan I, Hancock JW. Constraint-based failure assessment diagrams. Int J Pres Ves Piping 1995;64:287–98.
[15] O'Dowd NP, Shih CF. Two-parameter fracture mechanics: Theory and applications. Fract Mech 1994;24:21–47. ASTM STP 1207.

[16] Shih CF, O'Dowd NP, Kirk MT. A framework for quantifying crack tip constraint. Constr Effects Fract ASTM STP 1993;1171:2–20.
[17] O'Dowd NP. Applications of two parameter approaches in elastic–plastic fracture mechanics. Engng Fract Mech 1995;52:445–65.
[18] Bass BR, McAfee WJ, Williams PT, Pennell WE. Fracture assessment of shallow-flaw cruciform beams tested under uniaxial and biaxial loading conditions. Nuclear Engng Des 1999;188:259–88.
[19] English SA, Arakere NK. Effects of the strain-hardening exponent on two-parameter characterizations of surface-cracks under large-scale yielding. Int J Plast. doi:10.1016/j.ijplas.2010.10.002.
[20] Sharma SM, Aravas N, Zelman MG. Two-parameter characterization of crack tip fields in edged-cracked geometries: plasticity and creep solutions. Fract Mech 1995;25:309–27. ASTM STP 1220.
[21] Williams ML. On the stress distribution at the base of a stationary crack. J Appl Mech 1957;24:111–4.
[22] Systèmes Dassault. ABAQUS Ver. 6.7–4. Providence, RI: Dassault Systèmes; 2007.
[23] Gray DL, Moser DJ. Finite element analysis of a composite overwrapped pressure vessel. AIAA 2004-3506 2004.
[24] Quest Reliability LLC. FEA-Crack Ver. 3.1.56. Boulder, CO: Quest Reliability LLC; 2007.
[25] Betegón C, Hancock JW. Two-parameter characterization of elastic-plastic crack-tip fields. J Appl Mech 1991;58:104–10.
[26] Leach AM, Daniewicz SR, Newman Jr JC. A new constraint based fracture criterion for surface cracks. Engng Fract Mech 2007;74:1233–42.
[27] MacMaster FJ, Chan KS, Bergsma SC, Kassner ME. Aluminum alloy 6069 part II: fracture toughness of 6061-T6 and 6069-T6. Mater Sci Engng A289; 2000. p. 54–9.
[28] Rice JR, Tracey DM. On the enlargement of voids in triaxial stress field. J Mech Phys Solids 1974;17:201–17.
[29] Tvergaard V. On localization in ductile materials containing spherical voids. Int J Fract 1982;18:237–52.
[30] Garrison Jr WM, Moody NR. Ductile fracture. J Phys Chem Solids 1987;48:1035–74.
[31] Tvergaard V, Hutchinson JW. Two mechanisms of ductile fracture: void by void growth versus multiple void interaction. Int J of Solids Struct 2002;39:3581–97.